

Ligand-Induced Changes in the Structure and Dynamics of *Escherichia coli* Peptide Deformylase[†]

Carlos D. Amero,[‡] Douglas W. Byerly,[§] Craig A. McElroy,[§] Amber Simmons,^{||} and Mark P. Foster*,^{‡,§,||}

[‡]Biophysics Program and [§]Biochemistry Program and ^{||}Department of Biochemistry, The Ohio State University, Columbus, Ohio 43210

Received April 7, 2009; Revised Manuscript Received June 30, 2009

ABSTRACT: Peptide deformylase (PDF) is an enzyme that is responsible for removing the formyl group from nascently synthesized polypeptides in bacteria, attracting much attention as a potential target for novel antibacterial agents. Efforts to develop potent inhibitors of the enzyme have progressed on the basis of classical medicinal chemistry, combinatorial chemistry, and structural approaches, yet the validity of PDF as an antibacterial target hangs, in part, on the ability of inhibitors to selectively target this enzyme in favor of structurally related metallohydrolases. We have used ¹⁵N NMR spectroscopy and isothermal titration calorimetry to investigate the high-affinity interaction of EcPDF with actinonin, a naturally occurring potent EcPDF inhibitor. Backbone amide chemical shifts, residual dipolar couplings, hydrogen–deuterium exchange, and ¹⁵N relaxation reveal structural and dynamic effects of ligand binding in the immediate vicinity of the ligand-binding site as well as at remote sites. A comparison of the crystal structures of free and actinonin-bound EcPDF with the solution data suggests that most of the consequences of the ligand binding to the protein are lost or obscured during crystallization. The results of these studies improve our understanding of the thermodynamic global minimum and have important implications for structure-based drug design.

Peptide deformylase (PDF) is an essential and highly conserved enzyme that functions in protein maturation by removing the N-formyl group from the methionine of nascently synthesized polypeptides in bacteria, protists, and eukaryotic organelles (1–9). Because protein translation in bacteria is initiated with *N*-formylmethionine, PDF has emerged as a target of efforts to develop novel antibacterial agents (10–16). The extensively characterized enzyme from *Escherichia coli* (EcPDF)¹ exhibits some substrate selectivity in vitro (4, 6, 17–21); this property has guided the design of several effective substrate analogue inhibitors (18–23). Current work seeks to identify compounds with broad-spectrum activity against bacterial PDF while avoiding inhibition of other cellular targets, including the recently identified human mitochondrial protein (7, 9, 24).

As a member of the metallohydrolase superfamily that includes the matrix metalloproteins (MMPs) thermolysin and stromelysin (2–4), PDF binds divalent metals in a tetrahedral arrangement involving coordination with two histidines in a conserved QHExDH motif and a cysteine from a conserved EGCLS motif; a water molecule serves as the

fourth ligand (Figure 1). Although the active site metal in most members of the superfamily is zinc, evidence suggests the native metal in EcPDF is iron (5). Crystal structures of EcPDF free (25–27) and in complex with several competitive inhibitors capable of metal coordination have been reported (22, 23), as well as an NMR structure of the conserved catalytic core (residues 1–147) lacking the C-terminal helix, α 3 (2, 28, 29). In addition, crystal structures of PDF from several bacteria, including *Streptococcus pneumoniae*, *Staphylococcus aureus*, *Haemophilus influenzae*, *Pseudomonas aeruginosa*, and *Bacillus stearothermophilus* (13, 15, 30, 31), are now available as well as that of the protist *Plasmodium falciparum* (32).

In search of inhibitors of PDF, much work has focused on complexes of EcPDF with derivatives of actinonin (Figure 1B), a hydroxamic acid-containing actinomycete-derived natural product that serves as a competitive inhibitor (13, 23). The available crystal structures of free and actinonin-bound EcPDF revealed measurable, if subtle, structural differences between the free and bound state, suggesting that induced-fit recognition may play a role in inhibitor binding. Such protein plasticity is increasingly being recognized as obfuscating to structure-based drug design efforts (33) since it obscures the structure of the free energy minimum and makes it difficult to meaningfully predict thermodynamic relationships.

To improve our understanding of binding determinants for PDF, it is necessary to complement structural insight with dynamic and thermodynamic knowledge. In particular, isothermal titration calorimetry (ITC) can be used to directly measure the enthalpy of binding (ΔH_{bind}) and obtain the association equilibrium constant (K_A), from which the binding free energy (ΔG_{bind}) can be derived. The overall thermodynamics of ligand

*To whom correspondence should be addressed: Department of Biochemistry, The Ohio State University, 484 W. 12th Ave., Columbus, OH 43210. Phone: (614) 292-1377. Fax: (614) 292-6773. E-mail: foster.281@osu.edu.

[†]This work was supported in part by grants to M.P.F. from the American Heart Association/Ohio Valley Affiliate (AHA 0060418B) and the National Science Foundation (MCB 0092962). Abbreviations: EcPDF, *E. coli* peptide deformylase; NMR, nuclear magnetic resonance spectroscopy; rDC, residual dipolar coupling; ITC, isothermal titration calorimetry; CSA, chemical shift anisotropy; S^2 , square of the generalized order parameter from model-free analysis; H–D exchange, exchange of hydrogen (protons) with deuterium; rmsd, root-mean-square difference; PDB, Protein Data Bank.

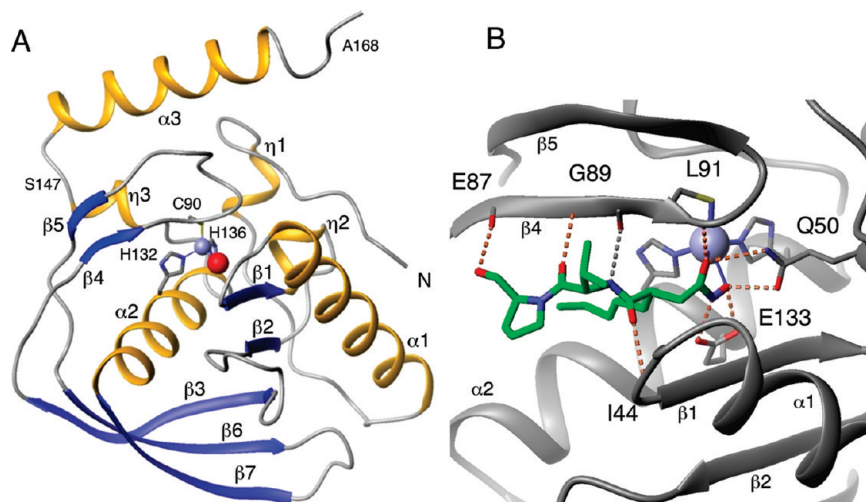


FIGURE 1: Peptide deformylase. (A) Ribbon diagram of the EcPDF crystal structure (PDB entry 1BS5, chain A). The bound metal is colored blue, and metal ligands are Cys⁹⁰, His¹³², and His¹³⁶; the oxygen atom from the water molecule that comprises the fourth metal ligand is shown as a red sphere. Ser¹⁴⁷ marks the C-terminus of the catalytic core used in this study. (B) Close-up of the actinonin binding site illustrating the intermolecular hydrogen bonds (dashes) and actinonin–metal interactions.

binding can be described by partitioning enthalpic and entropic contributions to the binding free energy:

$$\begin{aligned}\Delta G_{\text{bind}} &= \Delta H_{\text{bind}} - T\Delta S_{\text{bind}} \\ &= \Delta H_{\text{bind}} - T(\Delta S_{\text{solv}} + \Delta S_{\text{conf}} + \Delta S_{t/r})\end{aligned}$$

where ΔS_{bind} is the entropy change upon binding. The entropy term can be further partitioned into intermolecular and intramolecular components: ΔS_{solv} is the entropy change due to the changes in solvation of both binding partners, ΔS_{conf} is the conformational entropy change due to changes in structure and dynamics, while $\Delta S_{t/r}$ refers to changes in translational and rotational degrees of freedom (34). Formation of an enzyme–ligand complex is usually accompanied by an enthalpy gain through the formation of favorable intermolecular interactions (hydrogen bonds and van der Waals forces), but overall affinity is also affected by changes in conformational entropy at the binding interface, exclusion of ordered water molecules (hydrophobic effect), and gains in entropy at remote sites throughout the protein.

High-resolution NMR spectroscopy provides a means of observing and quantifying protein flexibility and the effect of ligand binding on protein structure in solution. For proteins weakly aligned in a magnetic field, residual dipolar couplings (rDCs) (35) provide a direct measurement of the orientation of individual bond vectors relative to the molecular frame, allowing ligand-induced structural changes to be precisely measured. Native state hydrogen–deuterium exchange measurements enable quantification of local protein flexibility and stability, yielding thermodynamic insights that could be used to dissect individual contributions to binding free energies (36–44). Moreover, heteronuclear relaxation rates (45) provide a measure of the amplitudes of bond-vector motions occurring on the nanosecond to picosecond time scales [the Lipari–Szabo order parameter, S^2 (46)] that can be used to estimate the conformational entropy of individual residues in the protein (36, 37), thus providing a means of better characterizing binding sites and quantifying the thermodynamic effect of ligand binding on the conformational entropy change, ΔS_{conf} , of the affected sites.

To gain insight into the role of protein flexibility in molecular recognition, we have characterized the effect of actinonin binding on the solution structure and dynamics of EcPDF using NMR

measurements of backbone rDCs, hydrogen–deuterium exchange rates, and ¹⁵N relaxation rates. Although we found a correlation between the proximity to the binding site and induced structural and dynamic changes, rDC measurements highlighted differences between the crystal and solution structures, while relaxation and H–D exchange rate data suggest that localized changes in structure, dynamics, and thermodynamics are transmitted to other parts of the protein. These data underscore the importance of understanding protein structure and dynamics in solution and demonstrate that local effects of ligand binding have consequences at remote sites in ways that are not entirely understood and are difficult to predict.

MATERIALS AND METHODS

Protein and Ligand Samples. The catalytic core of *E. coli* PDF (residues 1–147) (28) was expressed and purified as described previously (47). All experiments were performed with the conserved catalytic core of EcPDF (residues 1–147); for the sake of convenience, unless explicitly stated, EcPDF is used throughout the text to indicate this domain. Actinonin {3-[{(1-{[2-(hydroxymethyl)-1-pyrrolidinyl]carbonyl}-2-methylpropyl)carbamoyl]octanohydroxamic acid (CAS registry no. 13434-13-4)} (48) was generously provided by Z. Yuan (Versicor, Inc., San Diego, CA) or purchased (catalog no. A6671) from Sigma-Aldrich (St. Louis, MO) and used without further purification; purity and integrity were checked by electrospray mass spectrometry and one-dimensional WATERGATE (49, 50) NMR spectroscopy. NMR samples included 0.6–1.0 mM protein in 20 mM Tris (pH 7.2), 10 mM NaCl 10% D₂O, 90% H₂O, and 0.02% Na₃N; EcPDF–actinonin complex samples contained a slight excess of actinonin (~1.1 equiv).

Isothermal Titration Calorimetry. ITC experiments were performed at 37 °C on a MicroCal VP-ITC instrument, with the cell containing EcPDF at a concentration of 32–40 μM and the syringe containing 320–400 μM actinonin. Each experiment consisted of 59 injections of 5 μL of actinonin with a 240 s interval between each injection. The protein samples were dialyzed overnight, and the dialysate was used to dissolve the actinonin sample. Both experimental solutions were thoroughly degassed before each titration.

The data were analyzed using a one-site binding model with the Origin (V.7 SR4) software package (MicroCal, Inc.). The baselines at the beginning and end of each injection peak were adjusted manually. The last few points of the titration, after the solution was saturated, were averaged and subtracted from each data point to correct for the heat of dilution. Origin uses nonlinear least-squares minimization and the concentrations of the titrant, L_T , and the analyte, M_T , to fit the energy flow per injection, Q_i , to the equilibrium binding equation $K_A = \Theta / [(1 - \Theta)(L_T - n\Theta M_T)]$, where $\Theta_i = Q_i / (M_T V_0 n \Delta H)$ is the fraction bound after the i th injection and V_0 is the cell volume, generating best fit values of the stoichiometry (n), binding enthalpy (ΔH), and binding constant (K_A). The binding free energy is obtained from the relationship $\Delta G_{\text{bind}} = -RT \ln K_A = RT \ln K_D$, while the entropy of binding results from the Gibbs relation $\Delta G_{\text{bind}} = \Delta H_{\text{bind}} - T\Delta S_{\text{bind}}$.

The heat capacity change (ΔC_p) for binding of actinonin to EcPDF was obtained from ITC experiments performed at 13, 19, 25, 31, 37, and 43 °C, and a linear fit of the enthalpy change at each temperature to the equation $\Delta H = \Delta C_p(T - \Delta T_h)$, where T_h is the temperature at which the binding enthalpy is zero. Titrations were repeated at varying salt concentrations (10, 150, and 300 mM NaCl) to test for ion linkage, and in buffers with different ionization enthalpies [tris(hydroxymethyl)aminomethane (Tris; $h_{\text{ion}} = -11.3 \text{ kcal mol}^{-1}$), 4-(2-hydroxyethyl)-1-piperazineethanesulfonic acid (HEPES; $h_{\text{ion}} = -4.8 \text{ kcal mol}^{-1}$), and cacodylic acid ($h_{\text{ion}} = -0.7 \text{ kcal mol}^{-1}$)] to test for proton linkage. In all calculations, the differences between the standard state (1 M) and those of the NMR and ITC experiments were neglected.

NMR Spectroscopy. Backbone resonance assignments of free EcPDF were obtained from the BioMagResBank (accession number 4089) (2, 29) and verified by ^{15}N -separated TOCSY and NOESY spectra (51). ^{15}N chemical shifts were adjusted by +3 ppm to correct for a systematic offset (47) resulting from differences in referencing between the published work and that reported here. NMR data for resonance assignments were recorded at 310 K on Bruker DMX-600 or DRX-600 spectrometers equipped with triple-resonance three-axis shielded gradient probes. Proton chemical shifts were referenced externally to DSS (2,2-dimethylsilapentane-5-sulfonic acid), and ^{15}N and ^{13}C chemical shifts were referenced indirectly on the basis of their nuclear gyromagnetic ratios (52). Sequence-specific backbone assignments for H^{N} , N , C^{α} , C^{β} , and C' were made from HNCACB, CBCA(CO)NH, and HNCO spectra (52). Backbone assignments were further confirmed from the aliphatic side chain proton and carbon resonances, which were assigned by incorporating data from HBHA(CO)NH, HCCH-TOCSY, HCCH-COSY, ^{15}N -separated NOESY, ^{15}N -separated TOCSY, HNHA, ^{13}C -separated NOESY, and C(CO)NH-TOCSY spectra (51, 52). Time domain data were zero filled to twice the number of acquired points in all dimensions to improve spectral resolution. NMR data were processed with NMRPipe (53) and analyzed using NMRVIEW (54).

Weighted-average ^1H and ^{15}N shift perturbations induced by actinonin were examined by comparing peak positions in two-dimensional NMR spectra of free and actinonin-bound EcPDF and analyzed according to (55)

$$\Delta\delta_{\text{HN}} = \sqrt{\frac{\Delta\delta_{\text{H}}^2 + (\Delta\delta_{\text{N}}/5)^2}{2}}$$

where $\Delta\delta_{\text{H}}$ and $\Delta\delta_{\text{N}}$ are the changes in chemical shift for ^1H and ^{15}N , respectively.

NMR Relaxation Measurements. Relaxation spectra were recorded at a ^1H frequency of 600 and/or 800 MHz on spectrometers equipped with triple-resonance single-axis gradient cryoprobes. ^{15}N R_1 (longitudinal) and R_2 (transverse) relaxation rate constants were obtained from standard inversion recovery and CPMG-based experiments (45, 56) acquired with 16 scans per time point, with 2048×256 complex data points. The recovery delay for both experiments was 1.5 s. Nine relaxation time points were sampled in random order for each experiment (10, 50, 150, 300, 500, 750, 1000, 1500, and 2000 ms and 0, 17, 34, 51, 68, 85, 102, 136, and 187 ms for R_1 and R_2 , respectively). Data were zero-filled to 4096×512 in the direct and indirect dimensions, respectively, and apodized with a square cosine window function in the direct dimension and in the indirect dimension. Relaxation rates were obtained from one-parameter exponential fits to the peak intensities at each time point. The standard deviation of the baseline spectral noise was taken to be the uncertainty in peak heights, and uncertainties in the fit parameters were obtained from Monte Carlo simulations with a confidence interval of 0.68. Heteronuclear NOE spectra (57) were acquired (at 600 MHz) in an interleaved fashion with 32 scans per increment and a 5 s recycle delay. The NOE values were determined from the ratios of the peak intensities in spectra acquired with and without proton saturation. Proton saturation was achieved via a train of 120° proton pulses applied every 18 ms for the last 3 s of the recycle delay.

The relaxation data were analyzed in terms of the extended “model-free” formalism (58) using the relax software with a modified model-free optimization protocol (59), in which, prior to optimization of the diffusion tensor, model-free modes are determined. Residues 1–147 of the crystal structures of free EcPDF (PDB entry 1BS5, chain A) or the EcPDF–actinonin complex (residues 1–147 of PDB entry 1G2A, chain A), protonated with MOLMOL (60), were used to test the fitness of the data to various diffusion models. Amides were fit to models in which diffusion was assumed to be isotropic (spherical), axially symmetric (oblate and/or prolate), or fully anisotropic (ellipsoid), and the pairwise and overall fit of the data to each model was evaluated. The appropriateness of each model was evaluated by use of the Bayesian information criteria (BIC) (61) and 500 Monte Carlo simulations, as implemented in the program relax (62). A value of -172 ppm was used for the amide ^{15}N chemical shift anisotropy (CSA) and 1.02 Å for the N–H bond distance (63). For both free and actinonin-bound EcPDF, there was no significant improvement in the fit to anisotropic models over isotropic treatment.

The internal dynamics parameters for each amide resonance were obtained by fitting the experimental relaxation data to five different motional models. In accord with the extended model-free formalism (58), in addition to the common overall correlation time, τ_m , the parameters optimized for each model are (1) S^2 , (2) S^2 and τ_c , (3) S^2 and R_{ex} , (4) S^2 , τ_c , and R_{ex} , and (5) S_s^2 , S_s^2 , and τ_c , where R_{ex} is a phenomenological exchange term introduced to account for chemical exchange line broadening (affecting R_2) and τ_c is the effective correlation time for internal motions. The five models have the following implicit assumptions: (1) $S_s^2 = 1$ and $\tau_f \sim 0$, (2) $S_s^2 = 1$ and slower motions are negligible (i.e., $\tau_e = \tau_f$), (3 and 4) $R_{\text{ex}} > 0$, and (5) only $\tau_f \sim 0$. Model selection was performed on the basis of BIC scores (61). After residues with significant overlap for the free and actinonin complex had been excluded, motional parameters were obtained for 109 of the free and 104 of the bound non-proline residues (total of 141).

Ligand-induced conformational entropy changes, ΔS_{conf} , were estimated for each amide by assuming a “diffusion in a cone” motional model (37, 64) as described by

$$\Delta S_{\text{conf}} = -k_b N_A T \ln \left[\frac{3 - (1 + 8S_b)^{1/2}}{3 - (1 + 8S_f)^{1/2}} \right]$$

where S_f and S_b are the order parameters for the free and bound forms, respectively [i.e., $(S^2)^{1/2}$], k_b is Boltzman’s constant, N_A is Avogadro’s number, and T is the absolute temperature, 310 K for these measurements (for residues where $S^2 > 0.95$, S was set to 0.98). After considering residues whose amides could be measured for the free and bound form, the thermodynamic parameters were obtained for 97 residues.

Residual Dipolar Coupling Measurements. Residual dipolar couplings (rDCs) (35) of EcPDF and its complex with actinonin were measured from the difference in multiplet splittings of signals in two-dimensional (2D) IPAP spectra (65) recorded in isotropic solution and in 20 mg/mL *Pf1* phage (ASLA BIOTECH Ltd.). Spectra were recorded at 800 MHz with 2048 × 256 complex points and spectral widths of 12019 and 4865 Hz in the direct (^1H) and indirect (^{15}N) dimensions, respectively. The data were apodized with a cosine bell and zero filled to 4096 points in each dimension prior to Fourier transformation. Peak positions were obtained by least-squares fitting as implemented in NMRPipe (53); amides with significant multiplet overlap were excluded from the analysis. The magnitudes of the alignment tensors were estimated from a histogram of the rDC data (66), using the relation

$$\text{rDC} = S^2 D_a^{\text{NH}} \left[(3 \cos^2 \theta - 1) + \frac{3}{2} R \sin^2 \theta \cos 2\varphi \right]$$

where D_a^{NH} is the axial component of the residual dipolar coupling tensor, R is the rhombicity, and S^2 is the square of the experimentally determined order parameter; the values were confirmed with PALES (67), using as input the first chain of structures 1BS5 (residues 1–147) and 1G2A (residues 1–147) for free and actinonin-bound EcPDF, respectively. Only amides for which both upfield and downfield multiplet components could be resolved were considered for analysis. Error estimates were obtained by propagating the uncertainties in the peak positions of each resonance obtained from the ratio of the line width at half-height to the signal-to-noise ratio (35). To compare the rDC values of free and actinonin-bound EcPDF, rDC values were normalized by the axial component of the corresponding tensor.

Hydrogen–Deuterium Exchange. Protein samples for measurement of amide exchange rates were prepared by dilution of highly concentrated samples into a buffer containing 90% D_2O to final concentration of 0.8 mM. ^{15}N -edited HSQC spectra were recorded every hour for a 10 h exchange time course; each acquisition was 11 min. The first time point was approximately 15 min after exchange into D_2O . Data were recorded on a Bruker DRX 800 MHz spectrometer at 37 °C. Exchange rates were obtained by fitting peak intensities to a single-exponential function. Residues that exchanged within the first time point were assigned on the order of the fastest rate measured ($\sim 0.1 \text{ s}^{-1}$), and residues for which the intensity did not change more than 10% after 10 h were assigned the magnitude of the slowest rate measured (0.0001 s^{-1}).

Site-specific changes in thermodynamic stability due to actinonin binding were obtained from changes in hydrogen–deuterium exchange rates based on

$$\Delta\Delta G = -RT \ln \frac{k_c}{k_f} = -RT \ln \frac{P_c}{P_f}$$

where k_f and k_c are the measured exchange rates and P_f and P_c are the derived protection factors for free and actinonin-bound EcPDF, respectively (68).

Structure Thermodynamic Calculations. Solvent-accessible surface areas were determined from structures 1BS5 and 1G2A for free and actinonin-bound EcPDF using STC (version 5.3) (69). The solvation entropy predicted from the structural data was calculated from the change in ASA using

$$\Delta S_{\text{sol}}(T) = -0.45\Delta A_{\text{np}} \ln(T/384.15) + 0.26\Delta A_{\text{pol}} \ln(T/335.15)$$

where ΔA_{np} is the change in nonpolar accessible surface area upon binding and ΔA_{pol} is the change in polar accessible surface area (69).

Per residue differences in the average crystal structures of the free (PDB entry 1BS5) and actinonin-bound PDF (PDB entry 1G2A) were computed with MOLMOL (60). First, average coordinates were computed for each structure with three molecules in the asymmetric unit. Then, the rmsds between these averaged coordinates were computed. Averaged coordinates were used without further regularization.

UV–Visible Spectroscopy of Co^{2+} -Bound EcPDF. Absorption spectra were acquired on a Hewlett-Packard 8452A UV–visible diode array spectrophotometer at room temperature. Protein samples were 50 μM (in 20 mM Tris at pH 7.2 and 25 °C and 10 mM NaCl). The EcPDF–actinonin complex was formed by the addition of actinonin (45 μL of a 17 mM stock solution in water) to 1 mL of the protein sample, resulting in a slight excess of inhibitor.

RESULTS

Isothermal Titration Calorimetry. Isothermal titration calorimetry measurements of the binding of actinonin to zinc-loaded EcPDF in NMR buffer [20 mM Tris (pH 7.2) and 10 mM NaCl] revealed a single, enthalpically favorable (exothermic) binding event (Figure 2). This, in addition to unpublished findings (70), is consistent with expectations for the mode of actinonin binding; no evidence was found for thermodynamically distinct species of the enzyme (71). The enthalpy of actinonin binding (ΔH_{bind}) was measured to be $-1.644 \pm 0.012 \text{ kcal mol}^{-1}$ at 37 °C, and the fitted dissociation constant (K_d) is $110 \pm 15 \text{ nM}$; these results indicate a c value ($K_{\text{AM}}T$) of ca. 290, slightly above the ideal range for accurate fitting of K_A (72, 73). From the fitted parameters, we obtained a ΔG of $-9.8 \pm 1.3 \text{ kcal mol}^{-1}$ and a ΔS of $27 \pm 4 \text{ cal mol}^{-1} \text{ K}^{-1}$. The heat capacity change (ΔC_p) associated with actinonin binding to EcPDF was obtained from the temperature dependence of the enthalpy, yielding a value of $-180 \pm 10 \text{ cal mol}^{-1} \text{ K}^{-1}$.

To account for contributions by salt bridge formation to the measured thermodynamic parameters (74–76), the salt dependence of binding was examined by performing ITC experiments with a range of different salt concentrations; if the rearrangement of atoms in EcPDF involved the formation or disruption of a salt bridge, the binding affinity (K_A) of the reaction would change as the salt concentration increases due to ion linkage. From experiments at 10 mM NaCl, 150 mM NaCl, and 300 mM NaCl

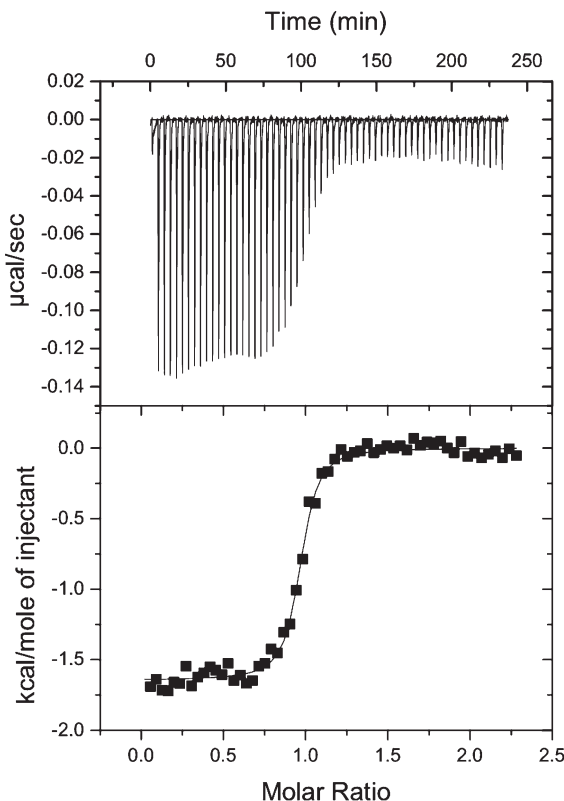


FIGURE 2: Isothermal titration calorimetry of Zn-bound PDF with actinonin at 37 °C. Heats of reaction from each injection were fit to a single-binding site model (Origin version 7) to yield the best fit values of binding stoichiometry ($n = 0.954 \pm 0.004$), affinity [$K_A = (9.02 \pm 1.2) \times 10^6 \text{ M}^{-1}$], and enthalpy ($\Delta H = -1.664 \pm 0.012 \text{ kcal mol}^{-1}$).

(Supporting Information), no significant correlation between salt concentration and binding affinity was apparent, implying that ion linkage does not contribute to the binding of actinonin to EcPDF.

Proton linkage (77) was examined by performing calorimetry experiments in buffers with different heats of ionization (78). In the event of proton linkage, the number of protons taken (or released) from the buffer can be calculated from (77)

$$\Delta H_{\text{obs}} = \Delta H_{\text{ind}} + n_{\text{H}} h_{\text{ion}}$$

where ΔH_{obs} is the measured enthalpy, ΔH_{ind} is the ionization-independent contribution, h_{ion} is the heat of ionization from the buffer, and n_{H} is the number of protons linked to the binding event. The change in enthalpy (Supporting Information) yielded an n_{H} value of 0.05 ± 0.02 , indicating that, at this pH, proton linkage does not significantly contribute to the thermodynamics of binding of EcPDF to actinonin. These controls indicated the measured thermodynamic parameters (i.e., ΔH_{bind} and ΔC_p) do not need to be corrected for ion or proton linkage.

Effect of Actinonin on the Structure of EcPDF. To examine the effects of actinonin binding to EcPDF, we performed a series of analyses of the atomic-level difference between the structural and dynamic properties of free and actinonin-bound EcPDF. The key findings are summarized in Figures 3 and 4 (and Supporting Information) and explained in detail below.

The crystal structures of EcPDF in the absence (PDB entry 1BS5, 2.5 Å resolution) (27) and presence of actinonin (PDB entry 1G2A, 1.75 Å) (23) were obtained from the same crystallographic space group, with three molecules per asymmetric unit. Comparison of the free and actinonin-bound structures was

complicated by the variability between molecules in the asymmetric unit. These differences mask the actinonin-induced changes in the structure of EcPDF. To distinguish structural variations due to crystal packing from those due to actinonin binding, the average structures for the free and bound proteins were separately calculated and compared. This analysis revealed a mean deviation of $0.23 \pm 0.11 \text{ \AA}$ for residues 1–147, $0.35 \pm 0.10 \text{ \AA}$ for the $\beta_4-\beta_5$ loop, and $0.27 \pm 0.12 \text{ \AA}$ for residues within 5 Å of the binding site (Glu⁴²–Ala⁴⁷, Gln⁵⁰, Ile⁸⁶–Ser⁹², Arg⁹⁷, Leu¹²⁵, Ile¹²⁸, Cys¹²⁹, His¹³², Glu¹³³, and His¹³⁶) (Figure 3A). Although they are not examined in detail here, it is worth noting that the ligand-induced structural perturbations are larger at the side chain level, with a mean displacement of $0.48 \pm 0.31 \text{ \AA}$ for all heavy atoms of residues in the proximity of the binding site (Supporting Information). However, since the NMR data reported below directly probe the backbone and not side chains, the analysis in this paper is limited to backbone atoms. Resonance assignments for actinonin-bound EcPDF were deposited in the BMRB under accession number 5404.

Resonance Assignments. Resonance assignments of the EcPDF–actinonin complex were determined from standard double- and triple-resonance NMR spectra, particularly three-dimensional HNCACB, CBCA(CO)NH, CC(CO)NH-TOCSY, HBHA(CO)NH, and HNCO spectra (51, 52). With the exception of the first residue, all amide proton and nitrogen chemical shifts of non-proline residues could be assigned. The high quality of the data allowed for the assignment of 99% of the H^N , C^α , C^β , H^α , H^β , and C' positions, including 140 backbone amide resonances (of 147 residues, six are prolines).

Spectral Perturbation Induced by Binding of Actinonin to EcPDF. Actinonin binding changes the coordination state of the bound metal. The substitution of Co^{2+} into the active site of metalloenzymes is a common method for characterizing binding events due to the metal's unique spectral properties (79). The electronic absorption spectrum in the visible region (d–d transitions) is sensitive to the coordination state of Co^{2+} and therefore a useful probe of the environment of the bound metal in EcPDF (80). Binding of actinonin to EcPDF results in a change in coordination state for the metal from tetrahedral to pentacoordinate, as the hydroxamate moiety of the ligand serves as a bidentate chelator of the bound metal, displacing the water molecule that serves as the found ligand in the free protein (13, 23). Consistent with this expectation, when actinonin binds we observe a decrease in absorption at 565 nm (Figure 5A).

Actinonin induces profound changes in the $^1\text{H}-^{15}\text{N}$ spectrum of the protein (Figure 5B) in spite of the small surface area buried by the ligand upon binding to EcPDF ($\sim 775.76 \text{ \AA}^2$), and the apparently subtle structural deformations. The weighted averages of the actinonin-induced shift perturbations are shown in Figure 3B and are mapped onto residues 1–147 of the crystal structure of the EcPDF–actinonin complex in Figure 4A. The correspondence between proximity to the ligand and shift perturbation is quite evident in the data. Clearly, the largest shift perturbations are concentrated in the immediate vicinity of the ligand-binding site, particularly, Glu⁴¹–Gly⁴⁷, Cys⁹⁰–Ser⁹², and His¹³² and Glu¹³³. However, significant shift perturbations are also evident at sites substantially removed ($> 8 \text{ \AA}$) from the site of actinonin binding [e.g., His⁷, Gln⁵⁵, Val¹⁰⁰, Phe¹⁴², and Met¹⁴³ (Figures 3B and 4)]. This finding was unexpected because of the subtle structural differences between the crystal structures of free and actinonin-bound EcPDF, and the absence of highly shielding or deshielding functionalities on actinonin.

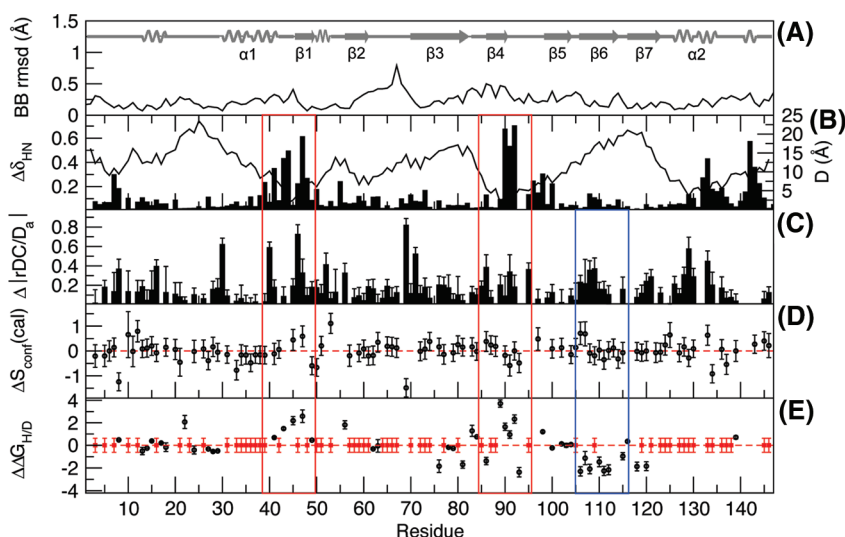


FIGURE 3: Effect of actinonin on the structure and dynamics of EcPDF. (A) Pairwise backbone atom rmsds among the mean structures from the three molecules in each of the asymmetric units of the free (PDB entry 1BS5) and actinonin-bound (PDB entry 1G2A) EcPDF crystal structures. (B) Weighted-average ^1H - ^{15}N shift perturbations, $\Delta\delta_{\text{HN}}$ (55), induced by actinonin (bars, left y-axis) graphed with intermolecular closest approach distance, D (lines, right y-axis). (C) Actinonin-induced absolute changes in residual dipolar couplings (rDC) recorded in 20 mg/mL *PfI* phage; rDC values were normalized by the magnitude of the alignment tensor (D_a) prior to subtraction (complex-free). (D) Actinonin-induced change in backbone entropy, ΔS (in entropy units, calories), as calculated from the change in order parameter S^2 (complex-free). Positive values indicate increased flexibility in the complex. (E) Actinonin-induced change in amide proton stability as measured from hydrogen–deuterium exchange data, with positive values indicating amides stabilized by actinonin binding; red symbols indicate residues whose amides exchange too fast or slow for the effect of actinonin to be measured. Red and blue boxes highlight regions close to and far from actinonin, respectively, for effects of the ligand are observed on ΔRDC , ΔS , ΔCS , and $\Delta\Delta G$.

The effect of actinonin binding on the residual dipolar couplings (rDCs) obtained under partial alignment obtained by addition of *PfI* filamentous phage was also assessed (Figure 5C), as was the degree of agreement between the observed rDC and those predicted on the basis of the crystal structures [PDB entries 1BS5 and 1G2A (Figure 5D)]; Q -factors (67) were 0.257 and 0.281 for chain A of free and actinonin-bound PDF, respectively. Because of the overlap of peak multiplets, ligand-dependent changes in rDC values could be obtained for 112 of 140 backbone amide resonances. Although care was taken to use identical conditions for sample preparation of the free and actinonin-bound EcPDF, the resulting alignment tensors differed slightly; the magnitudes of the alignment tensors (D_a^{NH}) were 2.33 and 2.01 for free and actinonin-bound EcPDF, with rhombicities (R) of 0.63 and 0.51, respectively.

After normalization of the measured rDC values by D_a^{NH} , the residual dipolar couplings of the free and actinonin-bound samples were compared (Figure 3C). Although the values were similar for the free and actinonin-bound states of the protein, significant differences (larger than twice the error) were noted for 35 residues, while significant changes were observed in residues within 5 Å of the ligand-binding site, especially near residues 43–50 and 126–136, but also at sites more remote from the binding site, such as residues 69–71 and 105–110. The actinonin-induced absolute changes in rDC values are mapped onto the structure of the EcPDF–actinonin complex in Figure 4B. Experimentally measured rDC values did not agree well with those calculated from the crystal structures (Figure 5D), as evident from the least-squares minimization of the target function

$$c = \sum_{ij} \left[\frac{(D_{ij}^{\text{meas}} - D_{ij}^{\text{calc}})^2}{\sigma_{ij}^2} \right]$$

of 7543 for free and 3146 for the complex, where D_{ij} is the rDC between pairs of spins and σ_{ij} is the uncertainty in the values (81).

Backbone Amide ^{15}N Relaxation. Backbone amide ^{15}N R_1 , R_2 , and NOE relaxation rate constants for free and actinonin-bound EcPDF are shown in the Supporting Information. High NOE values ($\eta > 0.8$) and relatively uniform R_2/R_1 ratios for both the free and actinonin-bound protein are indicative of a highly ordered structure throughout the core of the protein. Measurable actinonin-induced changes in the R_2/R_1 ratios are seen in the EGCLS motif (residues 88–92) and the QHExDH motif (residues 131–136), both of which are involved in metal binding. However, ligand-induced changes in relaxation rates were not limited to residues in or near the ligand-binding site.

Analysis of the ^{15}N relaxation for free EcPDF data resulted in a global rotational correlation time of 6.02 ns, with no significant improvement in the fit for anisotropic over isotropic treatments of molecular tumbling. The dynamics of 109 backbone amides could be investigated (of 140 possible, excluding the amino-terminal and proline residues). Of these, the relaxation rates for 69 amides were best fit by model 1 (S^2), 17 by model 2 (S^2 and τ_e), 14 by model 3 (S^2 and R_{ex}), five by model 4 (S^2 , τ_e , and R_{ex}), and four by model 5 (S_f^2 , S_s^2 , and τ_e).

Overall, the backbone of free EcPDF exhibits restricted mobility on the nanosecond to picosecond time scale, with an average S^2 of 0.86 ± 0.06 (Figure 6). Locally, the loop containing the conserved GxGLAAxQ motif (residues 43–50) and helix $\alpha 2$, bearing the QHExDH motif (residues 131–136), exhibit average or above average S^2 values. However, there are regions of the protein that are more flexible on this time scale, such as residues 97–102 in the loop between $\beta 4$ and $\beta 5$ near the actinonin binding site. Other residues displaying lower than average error-adjusted order parameters include Asp¹⁰, Asn²⁴, Glu⁶⁸, Arg⁹⁷, Arg¹⁰², Val¹⁰⁶, Lys¹⁰⁷, Asp¹²³, Gly¹²⁴, and the penultimate Leu¹⁴⁶ (Figure 6). Of the residues within 5 Å of the actinonin binding site or involved in metal binding, Ile⁴⁴, Gly⁴⁵, Leu⁴⁶, Glu⁸⁸, and Glu¹³³ required (R_{ex}) chemical exchange terms to fit the relaxa-

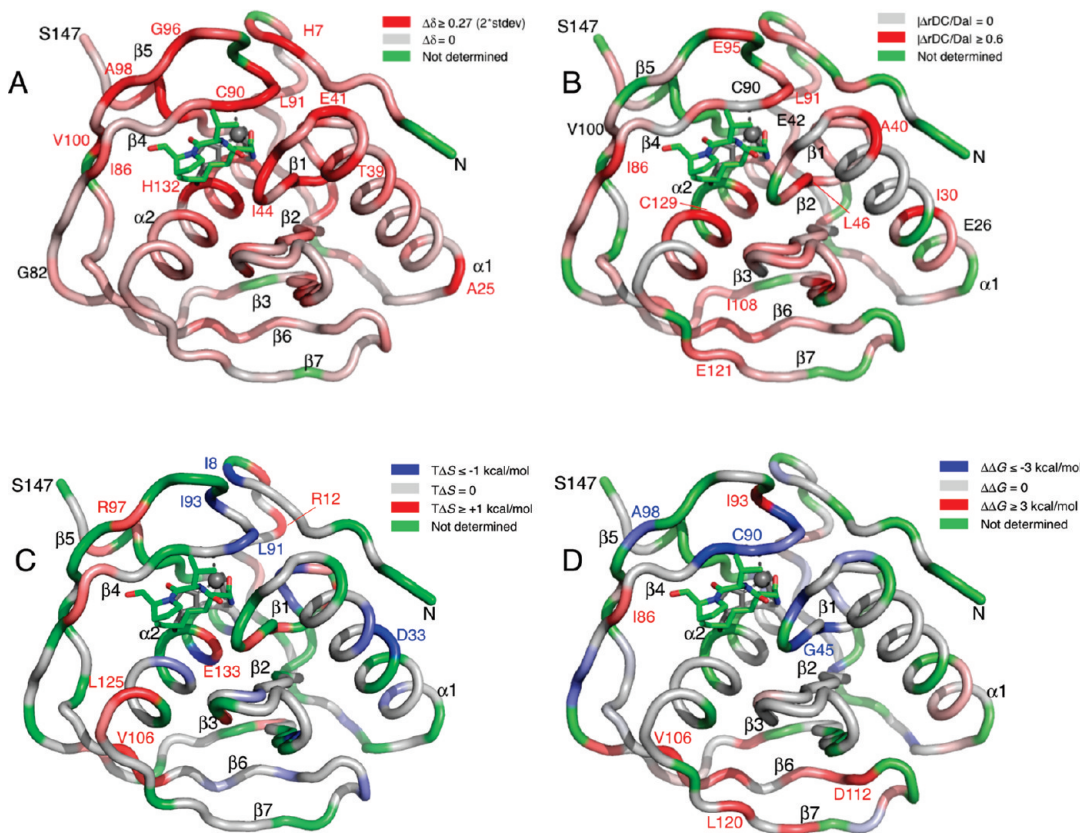


FIGURE 4: Effect of actinonin binding on EcPDF structure and dynamics. (A) Actinonin-induced amide shift perturbations. Residues are colored by a linear ramp from gray for unperturbed amides ($\Delta\delta = 0$) to red for amides perturbed greater than twice the standard deviation from the mean ($\Delta\delta > 0.27$). (B) Normalized actinonin-induced absolute changes in residual dipolar couplings ($|\Delta rDC|$). Values are mapped via a color ramp from gray (no change) to red ($|\Delta rDC| > 0.6$; ca. 3 times the standard deviation from the mean). (C) Change in residual conformational entropy, $T\Delta S$, mapped onto the crystal structure of the EcPDF–actinonin complex. Residues colored gray exhibit no measurable change in picosecond to nanosecond dynamics. Residues colored blue become more rigid upon actinonin binding. Residues colored red are more flexible in the complex. The magnitude of the change is represented by linear color ramps. (D) Change in free energy as reported by hydrogen–deuterium exchange rates. Residues colored gray exhibit no significant change in rate. Residues colored blue are residues whose amides are more protected in the complex. Residues colored red are less protected in the complex. The magnitude of the change is represented by linear color ramps. In all cases, values smaller than the error are colored gray in the figures. Residues colored green are those for which the data were not available either in the free protein or in the complex. The metal ion is drawn as a gray sphere; actinonin is shown as sticks with atoms colored by type.

tion data, while Gly⁴², Glu⁸⁷, and Glu⁸⁸ were best fit by including an internal correlation time (τ_e).

Model-free parameters for the actinonin–EcPDF complex were obtained for the 104 backbone amides; relaxation data of 73 amides were best fit by model 1, 20 by model 2, seven by model 3, two by model 4, and two by model 5. The overall nanosecond to picosecond dynamics of EcPDF in complex with actinonin is similar to that of the free protein, with an average S^2 of 0.86 ± 0.05 (Figure 6). In the complex, lower than average error-adjusted order parameters were still seen for Gln⁴, Asp¹⁰, Val¹⁶, Asn²⁴, Arg⁶⁹, Glu⁷⁹, Thr⁸⁴, Arg⁹⁷, Arg¹⁰², Asp¹²³, Gly¹²⁴, and the penultimate Leu¹⁴⁶, though most of the other residues near actinonin exhibit average or above average S^2 values. In the complex, the entirety of the central QHExDH-bearing helix $\alpha 2$ displays above average S^2 values except Gly¹²⁴, at the beginning of the helix, which is more dynamic than the average (Figure 6).

Although the protein experienced clear and measurable ligand-induced differences in the amplitudes of internal motions (Figure 3), the differences in S^2 values are relatively small, implying no large changes in the overall backbone dynamics. In all, 22 of 97 amides exhibited significant (error-adjusted) changes in order upon actinonin binding. Inspection of the differences in backbone order parameters (Figure 6 and the Supporting Information), or as translated to conformational

entropy and mapped onto the structure of the complex (Figure 4C), reveals decreased dynamics for Thr⁴⁹, Gln⁵⁰, Lue⁹¹, Ile⁹³, Met¹³⁴, and Leu¹³⁷, all of which are in the ligand-binding site. However, equally noteworthy are the increased dynamics both within the binding site and in other parts of the protein (e.g., Arg¹², Gly⁴⁵, Leu⁴⁷, Arg⁹⁷, Val¹⁰⁶, Leu¹²⁵, and Glu¹³³). It is clear from these observations that the effects of ligand binding are not limited to the residues immediately surrounding the binding cavity. In addition, several residues experience change in dynamics manifested by a decrease in the complexity of the model needed to describe their molecular motion. In particular, several residues do not contain an R_{ex} and τ_e term upon complex formation, which implies a change in motions on the microsecond to millisecond time scale (Figure 6).

Hydrogen–Deuterium Exchange. Backbone amide hydrogen–deuterium exchange rates under native conditions report on the local thermodynamic stability of protein folded states (68) and thus can be used to probe ligand-induced local stabilization. Deuterium exchange experiments show significant regions of both free EcPDF and actinonin-bound EcPDF for which backbone amides are completely protected from solvent and do not exchange after 10 h, as well as regions that are exposed to solvent and exchange within 20 min. Changes in the solvent exchange rate due to complex formation were obtained for 107 residues

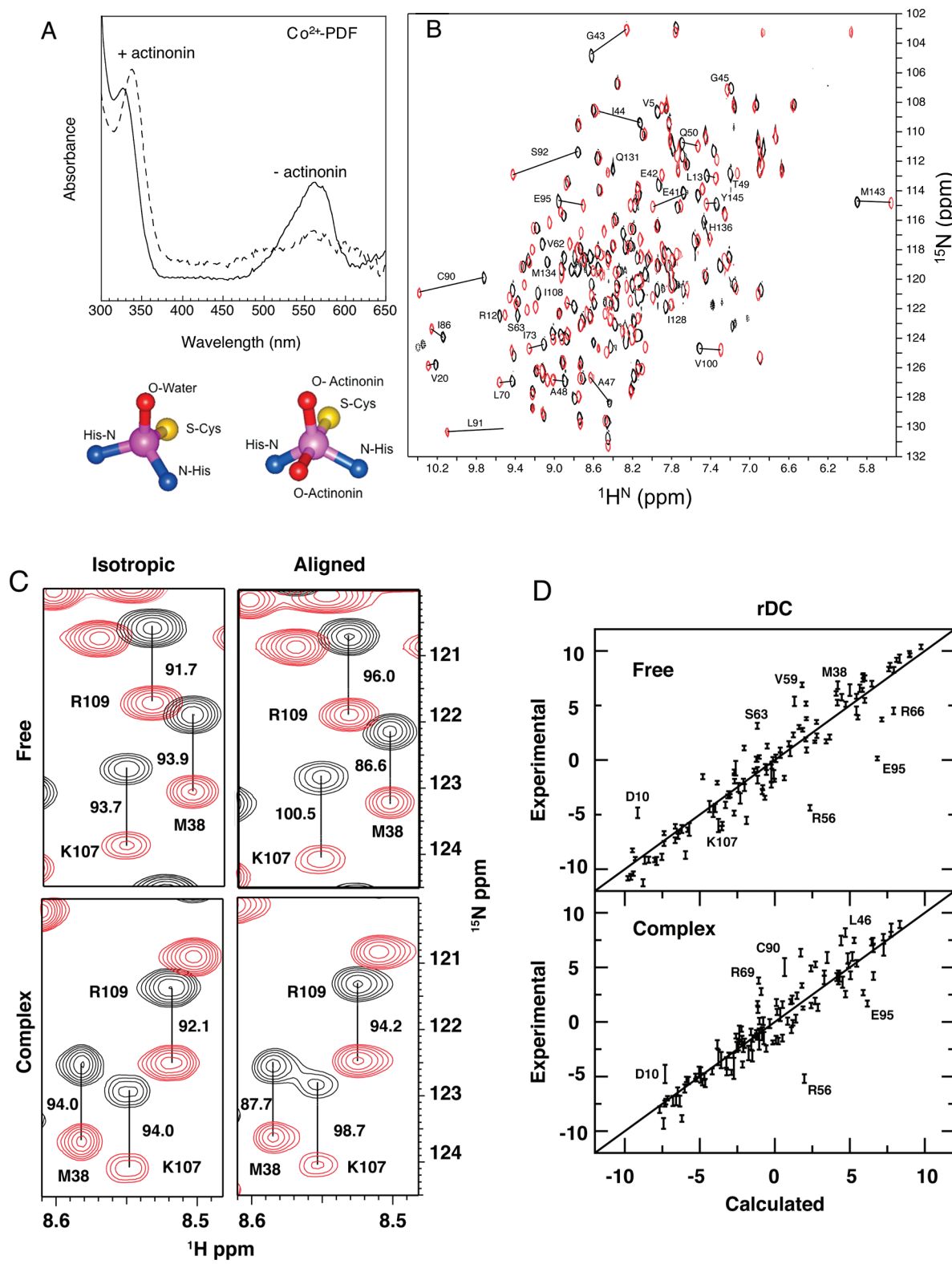


FIGURE 5: Spectral perturbations induced by actinonin binding. (A) UV-visible spectra of Co^{2+} -bound EcPDF recorded before (—) and after (---) addition of actinonin. The change in coordination geometry is evident from the decreased absorbance at 560 nm and the red shift of the band at 330 nm (79). (B) Overlay of 2D ^1H - ^{15}N HSQC spectra of (Zn^{2+}) EcPDF recorded in the absence (black) and presence (red) of stoichiometric concentrations of actinonin. (C) Expanded overlays of upfield (black) and downfield (red) components of IPAP spectra (800 MHz) showing the effect of actinonin binding on the rDCs of several amide resonances. The top two spectra correspond to IPAP spectra of free EcPDF recorded in an isotropic solution (left) or in 20 mg/mL *Pf1* phage, while the bottom two spectra are those of the complex. The amide resonances and splittings (in hertz) are as indicated; errors in peak positions were roughly ± 0.2 Hz. (D) Correlation plots showing the degree of agreement between experimentally measured rDCs and those calculated from the free (PDB entry 1BS5) and actinonin-bound (PDB entry 1G2A) crystal structures.

(Figure 3). Figure 4D shows the measured change in amide stability to exchange mapped to the structure of EcPDF.

As expected, actinonin binding resulted in significant protection from exchange for several residues within the ligand-binding

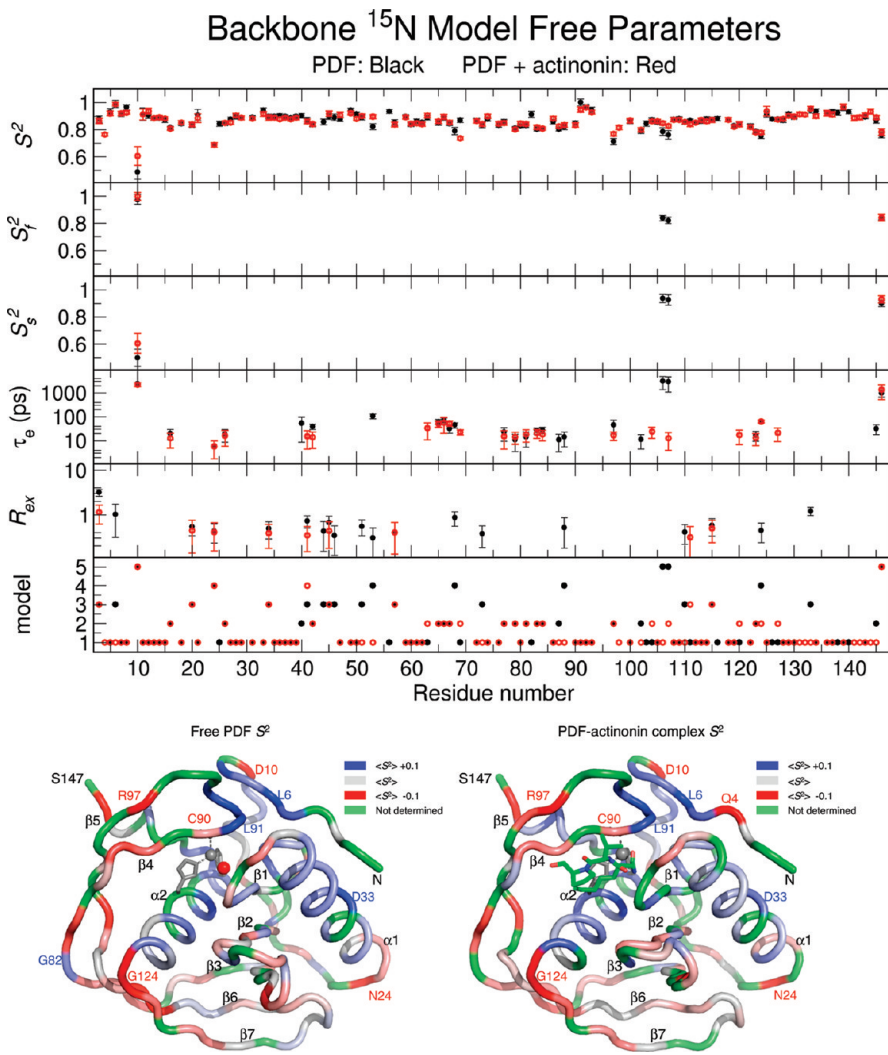


FIGURE 6: Backbone amide ^{15}N model-free parameters for free (black) and actinonin-bound EcPDF (red). Abbreviations: S^2 , square of the generalized order parameter; τ_e , effective correlation time for internal motions; R_{ex} , phenomenological exchange term contributing to line broadening; model, best fit extended model-free motional model selected for fitting relaxation data. The mean S^2 is 0.86 for the free protein and for the complex (dashed line), with standard deviations of 0.06 and 0.05, respectively. In the bottom panel, order parameters (S^2) for free EcPDF (left) and the EcPDF–actinonin complex (right) are mapped with linear color ramps from gray (mean S^2 for free PDF, 0.86) to red for amides more dynamic than the mean ($S^2 \leq 0.77$) or blue for amides more rigid than the average ($S^2 \geq 0.97$).

site, including Gly⁴³, Gly⁴⁵, Ala⁴⁷, Thr⁴⁹, Gly⁸⁹, Cys⁹⁰, Leu⁹¹, and Ser⁹² (Figures 3 and 4). However, these local stabilizing effects appear to be offset in part by destabilizing effects at remote sites in the protein (e.g., Ile²⁷, Gln²⁸, Arg²⁹, Val⁶², Glu⁷⁶, Leu⁷⁸, Glu⁷⁹, Ser⁸¹, Ile⁹³, Val¹⁰⁰, Val¹⁰⁶, Ile¹⁰⁸, Ala¹¹⁰, Leu¹¹¹, Asp¹¹², Gly¹¹⁵, Phe¹¹⁸, and Leu¹²⁰).

Structural Thermodynamics. Thermodynamic parameters associated with the release of water from the molecular surfaces (i.e., the hydrophobic effect) were estimated from the change in the exposed surface area of the crystal structures (69). The total change in accessible surface area for both the protein and ligand is 775.76 Å² (284.69 Å² polar and 491.07 Å² nonpolar), calculated using a solvent radius of 1.4 Å. The solvation entropy (ΔS_{sol}) was estimated to be 43 cal mol⁻¹ K⁻¹ ($T\Delta S = 13.3$ kcal mol⁻¹ K⁻¹ at 310 K). These same structure-based thermodynamic calculations predict an overall entropic contribution to binding, including entropy losses from changes in internal and overall rotational and translational degrees of freedom, of 7.8 kcal mol⁻¹ at 310 K (Supporting Information), which compares favorably to the calorimetrically measured value of 8.4 ± 1.3 kcal mol⁻¹.

DISCUSSION

Effect of Actinonin on the Structure of EcPDF. At the level of the peptide backbone, EcPDF is well-structured and rigid in the absence of ligands. This rigidity distinguishes EcPDF from related members of the broader metallohydrolase superfamily, many of which exhibit a high degree of protein flexibility at the level of the peptide backbone (33, 82). This difference may be related to the relatively narrow substrate specificity of PDF, for which the substrates are peptides bearing N-formylated methionine residues (21, 83), while other metallohydrolases have a broader range of substrates that may necessitate greater flexibility in the substrate binding site.

The crystal structure of the EcPDF-actinonin complex provides a high degree of detail into the atomic level interactions between the protein and inhibitor. Nevertheless, it is difficult to appreciate from this structure the extent to which which entropic effects contribute to binding. The large entropic effects of desolvation in the protein-ligand interface notwithstanding, the effects of the more subtle but concerted ligand-induced deformation on the thermodynamics of ligand

binding are difficult to appreciate from static structures. Indeed, the differences between molecules in the asymmetric unit are on the same order of magnitude as the differences between the free and ligand-bound protein (Supporting Information). Although backbone atom displacements are emphasized in this paper (since the NMR measurements employed here probe the backbone), the variability in the side chain displacements in the crystal structures follows a similar pattern, albeit with larger amplitudes.

The NMR chemical shift is very sensitive to local electronic effects, which depend on the equilibrium local structure and are sensitive to rapid conformational sampling. The strong correlation between the chemical shift data and distance to the ligand-binding site (Figures 3 and 4A) indicates that the largest ligand-induced changes occur in the immediate vicinity of the binding site. However, the NMR data also clearly show that ligand binding affects the structure of the protein at sites distant from the ligand-binding pocket; unfortunately, the chemical shift data alone do not reveal the nature of the change, since there is not a simple relationship between structure and chemical shift. Nevertheless, the chemical shift data suggest that structural changes are propagated from the ligand-binding site to remote sites, presumably via a network of interactions within the protein (main chain and/or side chain).

Residual dipolar couplings (rDCs) directly report the average orientation in solution of individual bond vectors (relative to the magnetic field). In a comparison of the crystallographic (Figure 3A) and rDC data (Figure 3C) it is clear that the crystallographic data fail to reveal some details of the structural changes induced by the ligand. The low correlation between the actinonin-induced shift perturbations and rDC data in solution, and the pairwise differences between the free and actinonin-bound structures in the crystal, suggest that some actinonin-dependent structural differences that are detected by the spectroscopic measurements in solution are lost to lattice constraints during crystallization (Figure 5D).

Effect of Actinonin on EcPDF Thermodynamics. Under native conditions [i.e., the EX2 regime (68)], hydrogen–deuteron exchange rates reflect local thermodynamic stability. As expected, there is an increase in stability for amides from residues adjacent to the site of actinonin binding (e.g., $\alpha 1-\beta 1$ and $\beta 4-\beta 5$). However, there are several regions of EcPDF for which binding of the ligand is destabilizing (i.e., experience increased H–D exchange rates), particularly in β -strands 3, 6, and 7, on the opposite side of the protein of the ligand-binding site (Figures 3 and 4). Thus, some of the local stabilizing effects seem to be countered by destabilization elsewhere in the protein.

An objective of this study was to use the changes in backbone ^{15}N order parameters (S^2) for individual backbone amides to obtain an estimate of the overall change in conformational entropy imposed by ligand binding (64). Model-free analysis of the backbone ^{15}N relaxation data has provided a map, albeit incomplete, of the residual entropy of EcPDF before and after binding of actinonin (Figures 3D and 4C). Two general features are noteworthy for this analysis (summarized in Figure 3D). First, the overall change in ΔS_{conf} is small. Of the 97 residues for which order parameters could be measured in both free and bound EcPDF, only 22 amides exhibit entropy changes ($T\Delta S_{\text{conf}}$) greater than the error in the measurements; averaged over all amides with changes greater than the error, the magnitude of $T\Delta S_{\text{conf}}$ is only $0.21 \text{ kcal mol}^{-1}$. Second, the local loss of conformational entropy is almost

entirely compensated by entropy gains at other sites. Thus, as measured from the picosecond to nanosecond dynamics of the backbone amides, given the experimental uncertainties, and ignoring the possible contribution from residues for which order parameters could not be measured, we found the net effect of actinonin binding on the overall conformational entropy of EcPDF to be negligible.

Conclusions. Successful structure-based inhibitor design requires knowledge of the local energy minimum defined by the structures and interactions of the target molecule and ligand. High-resolution structures derived from X-ray crystallography and NMR spectroscopy can provide a description of the local energy minimum and serve as templates for design. However, limited resolution, induced-fit binding, and structural plasticity complicate these objectives, partially because the structures provide limited insights into the steepness of the free energy well that surrounds this minimum, and thus little understanding of the cost of deformation of the conformation of the protein (or ligand) away from this target structure. Measurement of dynamics parameters (relaxation and rDCs) and H–D exchange rates for individual bond vectors can provide both important insights into the local energetic cost of deforming the equilibrium structure and a more accurate picture of the global minimum.

Experimental data show that the catalytic domain of EcPDF adopts a well-defined, globular structure that is held together by an interwoven network of intramolecular interactions. The site-specific measurements of the effect of actinonin binding on EcPDF (i.e., chemical shifts, backbone relaxation data, H–D exchange, and rDC) highlight significant perturbations in two regions: the ligand-binding site (residues 40–50 and 85–95) and on the opposite side of the protein, particularly in strand $\beta 6$ (Figures 3 and Figure 4). It is apparent from these observations that local structural perturbations in the binding site are transmitted via these interaction networks to other parts of the protein. The apparent rigidity of the PDF active site likely precludes a major role for induced fit in ligand binding, and may ultimately limit the selectivity of inhibitors of the enzyme. Nevertheless, the NMR measurements are acutely sensitive to these (even subtle) structural perturbations, providing unique insights into these interaction networks, and the shape of the global minimum.

The distribution of conformational entropy upon binding of actinonin to EcPDF appears to be consistent with the overall thermodynamic picture: that local loss of flexibility is offset by increased dynamics elsewhere in the protein. As a general disclaimer, however, we note that conclusions regarding the overall change in conformational entropy are limited by several factors. Among these are incomplete sampling (changes in order parameters could not be measured for all bond vectors in the protein), insufficient precision (changes that are smaller than the error in the measurements), and the implicit assumption that backbone motions are not correlated (thus representing independent degrees of freedom) (37). Further, this analysis is not sensitive to motions that do not reorient amide bond vectors relative to the molecular frame, entropy changes associated with conformational states sampled on slower time scales (greater than microseconds), and does not include changes in entropy associated with other bond vectors (i.e., those for which dynamics are not correlated to the backbone amides) throughout the enzyme.

In summary, assessment in EcPDF of actinonin-induced chemical shift perturbations and changes in backbone dynamics

reveals significant structural and dynamic effects at sites both adjacent to and remote from that of ligand binding. Comparison of rDC data for free and actinonin-bound EcPDF and to the crystal structures reveals changes in the equilibrium structure of EcPDF that are not detected in the crystalline state, presumably due to crystal packing forces. Finally, quantitation in EcPDF of the conformational entropy change that accompanies actinonin binding indicates that the net sum of the changes is small but measurable. This result is in agreement with previous findings that entropy changes can be readily redistributed from one site to another in a protein, with important thermodynamic implications. They underscore the premise that binding events are more complex than generally assumed and that an accurate descriptor of molecular behavior will need to incorporate both local and long-range contributions to the global energy minimum and the depth and width of the local potential energy well.

ACKNOWLEDGMENT

We thank R. Wilson, M. Chan, D. Pei, R. Rajagopalan, and Z. Yuan for reagents and helpful discussions and C. Cottrell and C. Yuan for help with NMR instrumentation.

SUPPORTING INFORMATION AVAILABLE

Tables of buffer ionization enthalpies and by-residue structure thermodynamic parameters, parameters and results of structure-based thermodynamic calculations, graphs of by-residue relaxation data, temperature-dependent enthalpy, salt dependence of ligand binding, representative best fit lines to relaxation data, H–D exchange, and order parameters. Protein sequence alignments, cartoon diagrams of free and actinonin-bound EcPDF, actinonin-induced displacements, order parameters mapped to the protein backbone, and a diagram of actinonin–PDF contacts. This material is available free of charge via the Internet at <http://pubs.acs.org>.

REFERENCES

- Mazel, D., Pochet, S., and Marliere, P. (1994) Genetic characterization of polypeptide deformylase, a distinctive enzyme of eubacterial translation. *EMBO J.* **13**, 914–923.
- Meinnel, T., Blanquet, S., and Dardel, F. (1996) A new subclass of the zinc metalloproteases superfamily revealed by the solution structure of peptide deformylase. *J. Mol. Biol.* **262**, 375–386.
- Meinnel, T., Lazennec, C., Villoing, S., and Blanquet, S. (1997) Structure-function relationships within the peptide deformylase family. Evidence for a conserved architecture of the active site involving three conserved motifs and a metal ion. *J. Mol. Biol.* **267**, 749–761.
- Rajagopalan, P. T., Datta, A., and Pei, D. (1997) Purification, characterization, and inhibition of peptide deformylase from *Escherichia coli*. *Biochemistry* **36**, 13910–13918.
- Rajagopalan, P. T. R., Yu, X. C., and Pei, D. (1997) Peptide deformylase: A new type of mononuclear iron protein. *J. Am. Chem. Soc.* **119**, 12418–12419.
- Ragusa, S., Mouchet, P., Lazennec, C., Dive, V., and Meinnel, T. (1999) Substrate recognition and selectivity of peptide deformylase. Similarities and differences with metzincins and thermolysin. *J. Mol. Biol.* **289**, 1445–1457.
- Bracchi-Ricard, V., Nguyen, K. T., Zhou, Y., Rajagopalan, P. T., Chakrabarti, D., and Pei, D. (2001) Characterization of an eukaryotic peptide deformylase from *Plasmodium falciparum*. *Arch. Biochem. Biophys.* **396**, 162–170.
- Giglione, C., Serero, A., Pierre, M., Boisson, B., and Meinnel, T. (2000) Identification of eukaryotic peptide deformylases reveals universality of N-terminal protein processing mechanisms. *EMBO J.* **19**, 5916–5929.
- Serero, A., Giglione, C., and Meinnel, T. (2001) Distinctive features of the two classes of eukaryotic peptide deformylases. *J. Mol. Biol.* **314**, 695–708.
- Meinnel, T. (2000) Peptide deformylase of eukaryotic protists: A target for new antiparasitic agents?. *Parasitol. Today* **16**, 165–168.
- Yuan, Z., Trias, J., and White, R. J. (2001) Deformylase as a novel antibacterial target. *Drug Discovery Today* **6**, 954–961.
- Apfel, C. M., Locher, H., Evers, S., Takacs, B., Hubschwerlen, C., Pirson, W., Page, M. G., and Keck, W. (2001) Peptide deformylase as an antibacterial drug target: Target validation and resistance development. *Antimicrob. Agents Chemother.* **45**, 1058–1064.
- Guilloteau, J.-P., Mathieu, M., Giglione, C., Blanc, V., Dupuy, A., Chevrié, M., Gil, P., Famechon, A., Meinnel, T., and Mikol, V. (2002) The crystal structures of four peptide deformylases bound to the antibiotic actinonin reveal two distinct types: A platform for the structure-based design of antibacterial agents. *J. Mol. Biol.* **320**, 951–962.
- Waller, A. S., and Clements, J. M. (2002) Novel approaches to antimicrobial therapy: Peptide deformylase. *Curr. Opin. Drug Discovery Dev.* **5**, 785–792.
- Smith, K. J., Petit, C. M., Aubart, K., Smyth, M., McManus, E., Jones, J., Fosberry, A., Lewis, C., Lonetto, M., and Christensen, S. B. (2003) Structural variation and inhibitor binding in polypeptide deformylase from four different bacterial species. *Protein Sci.* **12**, 349–360.
- Guay, D. R. (2007) Drug forecast: The peptide deformylase inhibitors as antibacterial agents. *Ther. Clin. Risk Manage.* **3**, 513–525.
- Meinnel, T., and Blanquet, S. (1995) Enzymatic properties of *Escherichia coli* peptide deformylase. *J. Bacteriol.* **177**, 1883–1887.
- Wei, Y., Yi, T., Huntington, K. M., Chaudhury, C., and Pei, D. (2000) Identification of a potent peptide deformylase inhibitor from a rationally designed combinatorial library. *J. Comb. Chem.* **2**, 650–657.
- Meinnel, T., Patiny, L., Ragusa, S., and Blanquet, S. (1999) Design and synthesis of substrate analogue inhibitors of peptide deformylase. *Biochemistry* **38**, 4287–4295.
- Huntington, K. M., Yi, T., Wei, Y., and Pei, D. (2000) Synthesis and antibacterial activity of peptide deformylase inhibitors. *Biochemistry* **39**, 4543–4551.
- Hu, Y. J., Wei, Y., Zhou, Y., Rajagopalan, P. T., and Pei, D. (1999) Determination of substrate specificity for peptide deformylase through the screening of a combinatorial peptide library. *Biochemistry* **38**, 643–650.
- Hao, B., Gong, W., Rajagopalan, P. T., Zhou, Y., Pei, D., and Chan, M. K. (1999) Structural basis for the design of antibiotics targeting peptide deformylase. *Biochemistry* **38**, 4712–4719.
- Clements, J. M., Beckett, R. P., Brown, A., Catlin, G., Lobell, M., Palan, S., Thomas, W., Whittaker, M., Wood, S., Salama, S., Baker, P. J., Rodgers, H. F., Barvin, V., Rice, D. W., and Hunter, M. G. (2001) Antibiotic activity and characterization of BB-3497, a novel peptide deformylase inhibitor. *Antimicrob. Agents Chemother.* **45**, 563–570.
- Boularot, A., Giglione, C., Petit, S., Duroc, Y., Alves de Sousa, R., Larue, V., Cresteil, T., Dardel, F., Artaud, I., and Meinnel, T. (2007) Discovery and refinement of a new structural class of potent peptide deformylase inhibitors. *J. Med. Chem.* **50**, 10–20.
- Chan, M. K., Gong, W., Rajagopalan, P. T., Hao, B., Tsai, C. M., and Pei, D. (1997) Crystal structure of the *Escherichia coli* peptide deformylase. *Biochemistry* **36**, 13904–13909.
- Becker, A., Schlichting, I., Kabsch, W., Groche, D., Schultz, S., and Wagner, A. F. (1998) Iron center, substrate recognition and mechanism of peptide deformylase. *Nat. Struct. Biol.* **5**, 1053–1058.
- Becker, A., Schlichting, I., Kabsch, W., Schultz, S., and Wagner, A. F. (1998) Structure of peptide deformylase and identification of the substrate binding site. *J. Biol. Chem.* **273**, 11413–11416.
- Meinnel, T., Lazennec, C., Dardel, F., Schmitter, J. M., and Blanquet, S. (1996) The C-terminal domain of peptide deformylase is disordered and dispensable for activity. *FEBS Lett.* **385**, 91–95.
- Dardel, F., Ragusa, S., Lazennec, C., Blanquet, S., and Meinnel, T. (1998) Solution structure of nickel-peptide deformylase. *J. Mol. Biol.* **280**, 501–513.
- Baldwin, E. T., Harris, M. S., Yem, A. W., Wolfe, C. L., Vosters, A. F., Curry, K. A., Murray, R. W., Bock, J. H., Marshall, V. P., Cialdella, J. I., Merchant, M. H., Choi, G., and Deibel, M. R., Jr. (2002) Crystal structure of type II peptide deformylase from *Staphylococcus aureus*. *J. Biol. Chem.* **277**, 31163–31171.
- Harris, M. S., Bock, J. H., Choi, G., Cialdella, J. S., Curry, K. A., Deibel, M. R., Jr., Jacobsen, E. J., Marshall, V. P., Murray, R. W., Jr., Vosters, A. F., Wolfe, C. L., Yem, A. W., and Baldwin, E. T. (2002) Co-crystallization of *Staphylococcus aureus* peptide deformylase (PDF) with potent inhibitors. *Acta Crystallogr. D58*, 2153–2156.
- Kumar, A., Nguyen, K. T., Srivathsan, S., Ornstein, B., Turley, S., Hirsh, I., Pei, D., and Hol, W. G. J. (2002) Crystals of peptide

- deformylase from *Plasmodium falciparum* reveal critical characteristics of the active site for drug design. *Structure* 10, 357–367.
33. Moy, F. J., Chanda, P. K., Chen, J., Cosmi, S., Edris, W., Levin, J. I., Rush, T. S., Wilhelm, J., and Powers, R. (2002) Impact of mobility on structure-based drug design for the MMPs. *J. Am. Chem. Soc.* 124, 12658–12659.
 34. Spolar, R. S., and Record, M. T., Jr. (1994) Coupling of local folding to site-specific binding of proteins to DNA. *Science* 263, 777–784.
 35. Bax, A., Kontaxis, G., and Tjandra, N. (2001) Dipolar couplings in macromolecular structure determination. *Methods Enzymol.* 339, 127–174.
 36. Li, Z., Raychaudhuri, S., and Wand, A. J. (1996) Insights into the local residual entropy of proteins provided by NMR relaxation. *Protein Sci.* 5, 2647–2650.
 37. Yang, D., and Kay, L. E. (1996) Contributions to conformational entropy arising from bond vector fluctuations measured from NMR-derived order parameters: Application to protein folding. *J. Mol. Biol.* 263, 369–382.
 38. Stivers, J. T., Abeygunawardana, C., and Mildvan, A. S. (1996) ¹⁵N NMR relaxation studies of free and inhibitor-bound 4-oxalocrotonate tautomerase: Backbone dynamics and entropy changes of an enzyme upon inhibitor binding. *Biochemistry* 35, 16036–16047.
 39. Kay, L. E., Muhandiram, D. R., Wolf, G., Shoelson, S. E., and Forman-Kay, J. D. (1998) Correlation between binding and dynamics at SH2 domain interfaces. *Nat. Struct. Biol.* 5, 156–163.
 40. Stone, M. J. (2001) NMR relaxation studies of the role of conformational entropy in protein stability and ligand binding. *Acc. Chem. Res.* 34, 379–388.
 41. Olejniczak, E. T., Zhou, M. M., and Fesik, S. W. (1997) Changes in the NMR-derived motional parameters of the insulin receptor substrate 1 phosphotyrosine binding domain upon binding to an interleukin 4 receptor phosphopeptide. *Biochemistry* 36, 4118–4124.
 42. Lee, A. L., Sharp, K. A., Kranz, J. K., Song, X. J., and Wand, A. J. (2002) Temperature dependence of the internal dynamics of a calmodulin-peptide complex. *Biochemistry* 41, 13814–13825.
 43. Kovrigin, E. L., Cole, R., and Loria, J. P. (2003) Temperature dependence of the backbone dynamics of ribonuclease A in the ground state and bound to the inhibitor 5'-phosphothymidine (3'-5')pyrophosphate adenosine 3'-phosphate. *Biochemistry* 42, 5279–5291.
 44. Arumugam, S., Gao, G., Patton, B. L., Semenchenko, V., Brew, K., and Van Doren, S. R. (2003) Increased backbone mobility in β -barrel enhances entropy gain driving binding of N-TIMP-1 to MMP-3. *J. Mol. Biol.* 327, 719–734.
 45. Kay, L. E., Torchia, D. A., and Bax, A. (1989) Backbone dynamics of proteins as studied by ¹⁵N inverse detected heteronuclear NMR spectroscopy: Application to staphylococcal nuclease. *Biochemistry* 28, 8972–8979.
 46. Lipari, G., and Szabo, A. (1982) A model-free approach to the interpretation of nuclear magnetic resonance relaxation in macromolecules. 1. Theory and range of validity. *J. Am. Chem. Soc.* 104, 4546–4559.
 47. Byerly, D. W., McElroy, C. A., and Foster, M. P. (2002) Mapping the surface of *Escherichia coli* peptide deformylase by NMR with organic solvents. *Protein Sci.* 11, 1850–1853.
 48. Gordon, J. J., Devlin, J. P., East, A. J., Ollis, W. D., Wright, D. E., and Ninet, L. (1975) Studies concerning the antibiotic actinonin. Part I. The constitution of actinonin. A natural hydroxamic acid with antibiotic activity. *J. Chem. Soc., Perkin Trans. 1*, 819–825.
 49. Piotto, M., Saudek, V., and Sklenar, V. (1992) Gradient-tailored excitation for single-quantum NMR spectroscopy of aqueous solutions. *J. Biomol. NMR* 2, 661–665.
 50. Sklenar, V., Piotto, M., Leppik, R., and Saudek, V. (1993) Gradient-tailored water suppression for ¹H-¹⁵N HSQC experiments optimized to retain full sensitivity. *J. Magn. Reson., Ser. A* 102, 241–245.
 51. Sattler, M., Schleucher, J., and Griesinger, C. (1999) Heteronuclear multidimensional NMR experiments for the structure determination of proteins in solution employing pulsed field gradients. *Prog. Nucl. Magn. Reson. Spectrosc.* 34, 93–158.
 52. Cavanagh, F. P. S. R. (2006) Protein NMR Spectroscopy: Principles and Practice , Academic Press, New York.
 53. Delaglio, F., Grzesiek, S., Vuister, G. W., Zhu, G., Pfeifer, J., and Bax, A. (1995) NMRPipe: A multidimensional spectral processing system based on UNIX pipes. *J. Biomol. NMR* 6, 277–293.
 54. Johnson, B. A. (2004) Using NMRView to visualize and analyze the NMR spectra of macromolecules. *Methods Mol. Biol.* 278, 313–352.
 55. Grzesiek, S., Bax, A., Clore, G. M., Gronenborn, A. M., Hu, J. S., Kaufman, J., Palmer, I., Stahl, S. J., and Wingfield, P. T. (1996) The solution structure of HIV-1 Nef reveals an unexpected fold and permits delineation of the binding surface for the SH3 domain of Hck tyrosine protein kinase. *Nat. Struct. Biol.* 3, 340–345.
 56. Barbato, G., Ikura, M., Kay, L. E., Pastor, R. W., and Bax, A. (1992) Backbone dynamics of calmodulin studied by ¹⁵N relaxation using inverse detected two-dimensional NMR spectroscopy: The central helix is flexible. *Biochemistry* 31, 5269–5278.
 57. LeMaster, D. M., Kay, L. E., Brunger, A. T., and Prestegard, J. H. (1988) Protein dynamics and distance determination by NOE measurements. *FEBS Lett.* 236, 71–76.
 58. Clore, G. M., Szabo, A., Bax, A., Kay, L. E., Driscoll, P. C., and Gronenborn, A. M. (1990) Deviations from the simple two-parameter model-free approach to the interpretation of nitrogen-15 nuclear magnetic relaxation of proteins. *J. Am. Chem. Soc.* 112, 4989–4991.
 59. d'Auvergne, E. J., and Gooley, P. R. (2008) Optimisation of NMR dynamic models II. A new methodology for the dual optimisation of the model-free parameters and the Brownian rotational diffusion tensor. *J. Biomol. NMR* 40, 121–133.
 60. Koradi, R., Billeter, M., and Wuthrich, K. (1996) MOLMOL: A program for display and analysis of macromolecular structures. *J. Mol. Graphics* 14, 51–55, 29–32.
 61. d'Auvergne, E. J., and Gooley, P. R. (2003) The use of model selection in the model-free analysis of protein dynamics. *J. Biomol. NMR* 25, 25–39.
 62. d'Auvergne, E. J., and Gooley, P. R. (2008) Optimisation of NMR dynamic models I. Minimisation algorithms and their performance within the model-free and Brownian rotational diffusion spaces. *J. Biomol. NMR* 40, 107–119.
 63. Palmer, A. G., III. (2001) Nmr probes of molecular dynamics: Overview and comparison with other techniques. *Annu. Rev. Biophys. Biomol. Struct.* 30, 129–155.
 64. Yang, D., Mok, Y. K., Forman-Kay, J. D., Farrow, N. A., and Kay, L. E. (1997) Contributions to protein entropy and heat capacity from bond vector motions measured by NMR spin relaxation. *J. Mol. Biol.* 272, 790–804.
 65. Ottiger, M., Delaglio, F., and Bax, A. (1998) Measurement of J and dipolar couplings from simplified two-dimensional NMR spectra. *J. Magn. Reson.* 131, 373–378.
 66. Clore, G. M., Gronenborn, A. M., and Bax, A. (1998) A robust method for determining the magnitude of the fully asymmetric alignment tensor of oriented macromolecules in the absence of structural information. *J. Magn. Reson.* 133, 216–221.
 67. Zweckstetter, M. (2006) Prediction of charge-induced molecular alignment: Residual dipolar couplings at pH 3 and alignment in surfactant liquid crystalline phases. *Eur. Biophys. J.* 35, 170–180.
 68. Dempsey, C. E. (2001) Hydrogen exchange in peptides and proteins using NMR spectroscopy. *Prog. Nucl. Magn. Reson. Spectrosc.* 39, 135–170.
 69. Lavigne, P., Bagu, J. R., Boyko, R., Willard, L., Holmes, C. F., and Sykes, B. D. (2000) Structure-based thermodynamic analysis of the dissociation of protein phosphatase-1 catalytic subunit and microcystin-LR docked complexes. *Protein Sci.* 9, 252–264.
 70. Simmons, A. (2007) Inhibition and thermodynamics of *Escherichia coli* peptide deformylase. B.S. Thesis, Department of Biochemistry, The Ohio State University, Columbus, OH.
 71. Berg, A. K., and Srivastava, D. K. (2009) Delineation of alternative conformational states in *Escherichia coli* peptide deformylase via thermodynamic studies for the binding of actinonin. *Biochemistry* 48, 1584–1594.
 72. Wiseman, T., Williston, S., Brandts, J. F., and Lin, L. N. (1989) Rapid measurement of binding constants and heats of binding using a new titration calorimeter. *Anal. Biochem.* 179, 131–137.
 73. Jelesarov, I., and Bosshard, H. R. (1999) Isothermal titration calorimetry and differential scanning calorimetry as complementary tools to investigate the energetics of biomolecular recognition. *J. Mol. Recognit.* 12, 3–18.
 74. Missimer, J. H., Steinmetz, M. O., Baron, R., Winkler, F. K., Kammerer, R. A., Daura, X., and van Gunsteren, W. F. (2007) Configurational entropy elucidates the role of salt-bridge networks in protein thermostability. *Protein Sci.* 16, 1349–1359.
 75. Tsumoto, K., Ogasahara, K., Ueda, Y., Watanabe, K., Yutani, K., and Kumagai, I. (1996) Role of salt bridge formation in antigen-antibody interaction. Entropic contribution to the complex between hen egg white lysozyme and its monoclonal antibody HyHEL10. *J. Biol. Chem.* 271, 32612–32616.
 76. Prabhu, N. V., and Sharp, K. A. (2005) Heat capacity in proteins. *Annu. Rev. Phys. Chem.* 56, 521–548.

77. Baker, B. M., and Murphy, K. P. (1996) Evaluation of linked protonation effects in protein binding reactions using isothermal titration calorimetry. *Biophys. J.* 71, 2049–2055.
78. Goldberg, R. N., Kishore, N., and Lennen, R. M. (2002) Thermodynamic Quantities for the Ionization Reactions of Buffers. *J. Phys. Chem. Ref. Data* 31, 231–370.
79. Maret, W., and Vallee, B. L. (1993) Cobalt as probe and label of proteins. *Methods Enzymol.* 226, 52–71.
80. Rajagopalan, P. T., Grimme, S., and Pei, D. (2000) Characterization of cobalt(II)-substituted peptide deformylase: Function of the metal ion and the catalytic residue Glu-133. *Biochemistry* 39, 779–790.
81. Dosset, P., Hus, J. C., Marion, D., and Blackledge, M. (2001) A novel interactive tool for rigid-body modeling of multi-domain macromolecules using residual dipolar couplings. *J. Biomol. NMR* 20, 223–231.
82. Cuniasse, P., Devel, L., Makaritis, A., Beau, F., Georgiadis, D., Matziari, M., Yiotakis, A., and Dive, V. (2005) Future challenges facing the development of specific active-site-directed synthetic inhibitors of MMPs. *Biochimie* 87, 393–402.
83. Ragusa, S., Mouchet, P., Lazennec, C., Dive, V., and Meinnel, T. (1999) Substrate recognition and selectivity of peptide deformylase. Similarities and differences with metzincins and thermolysin. *J. Mol. Biol.* 289, 1445–1457.